Radiocatalytic Cu-incorporated TiO 2 nano-particles for the degradation of organic species under gamma irradiation

L. Samet, K. March, O. Stephan, N. Brun, F. Hosni, F. Bessousa, J. Benasseur, R. Chtourou

Radiocatalytic Cu-incorporated TiO_2 nano-particles for the degradation of organic species under gamma irradiation

L. Samet[1,2,*], K. March[3], O. Stephan[3], N. Brun[3], F. Hosni[4], F. Bessousa[2], J. Benasseur[2], R. Chtourou[2]

[1]*Institut Préparatoire aux Etudes d'Ingénieurs d'El-Manar, Université Tunis El Manar, Campus Universitaire Farhat Hached d'El-Manar 2092 El Manar, Tunis, Tunisia.*

[2]*Laboratoire de Nanomatériaux et Systèmes pour les Energies Renouvelables, Centre de Recherches et des Technologies de l'Energie, Technopole Borj Cedria, Bp 95, hammammlif 2050, Tunisia.*

[3]*Laboratoire de Physique des Solides, UMR 8502 CNRS - Université Paris-Sud, Bât 510, 91405 Orsay cedex France.*

[4]*Laboratoire de Recherche en Energie et Matière pour le Développement des Sciences Nucléaires, Centre National des Sciences et Technologie Nucléaires, 2020 Sidi-Thabet, Tunisia.*

**Corresponding author:lolwa.samet@ipeiem.utm.tn*

ABSTRACT

We report on an experimental study aimed at optimizing the radiocatalytic properties of pure and copper-incorporated TiO_2 powders. This has been achieved by conducting cross-checked structural, optical and radiocatalytic studies. Structural and nanoscale analyses show evidence of internal doping by Cu^{2+} in the TiO_2 lattice that leads to the reduction of the optical band gap down to 1.5 eV. The effect of gamma radiation on the radiocatalytic activity of these catalysts was studied by degradation of methylene blue as a model pollutant. It was found that the addition of Cu-doped TiO_2 (anatase) powders improves significantly the pollutant degradation, as compared to photocatalysis. The doping and the annealing temperature's impact on the structural, optical and radiocatalytic efficiencies are highlighted and correlated.

Keywords: Copper-doped titania, Structure, Optical and radiocatalytic relationship, ELNES.

1. Introduction

Water is a scarce resource and wastewater is a major environmental problem. Advanced oxidation processes, like photocatalysis and radiocatalysis, are widely studied for the treatment of persistent organic compounds. Among several semiconductors used as heterogeneous photocatalysts and radiocatalysts, titanium dioxide (TiO_2) is the most widely used and has been intensively studied thanks to its many promising properties [1-37]. It presents a high chemical and mechanical stability and is amongst the synthetic nanoparticles that present especially interesting properties in the fields of nanotechnology, sustainable development and ecology. Titanium dioxide is a semiconductor that can only be activated with light of energy higher than about 3.2 eV or 3.0 eV for the anatase and rutile structures respectively. When TiO_2 is subjected to illumination, the electron-hole pairs formed can be trapped by surface hydroxyl groups. In the presence of oxygen and water, the trapped carriers form free radicals that are strong oxidizing species and are likely to mineralize organic pollutants. In this respect, the efficiency of TiO_2 catalysis needs to be further improved. Many strategies, such as doping [5-18], co-doping [20, 21], surface treatment [22], coupling with noble metal nanoparticles [23] or other semiconductors [24, 25], synthesis of nanomaterials with different morphologies [26], have been tried over the last few decades, in order to reduce the electron–hole recombination rate and improve the photocatalytic efficiency of TiO_2. Titanium dioxide has a high oxidation power so is easily doped with active ions. It has been shown that doping with transition metal cations is an efficient way of promoting the photocatalytic activity [16-18]. Such doping can extend the light absorption range from the UV down to the visible by inducing additional energy levels within the band gap, leading to the improvement of the TiO_2 photo-response. Several investigations on doped TiO_2 have succeeded in providing some indication about the substitutional or interstitial dopant location and its impact on the physical and electronic structure of TiO_2 [27, 28]. Doping with copper

appears to be a particularly promising approach for photocatalytic applications [18]. For example, it has been found that the incorporation of Cu^{2+} ions into a TiO_2 matrix can substitute for Ti^{4+} and/or segregate to the surface of TiO_2 crystallites in the form of CuO, Cu_2O or metallic Cu [14, 29-32] and improve significantly the photocatalytic activity. Theoretical investigations show that Cu doping can effectively narrow the band gap by creating impurity bands [15, 21], and thus improve the absorption of visible light in photocatalytic reactions. Alternatively, Wu and al. [33] reported that the dissolution of Cu ions in the TiO_2 lattice leads to a reduction in photocatalytic activity. It is now admitted that a compromise must be achieved between the band gap value and charge transfer at the surface of TiO_2 catalysts. However, the nature of the active copper species (CuO, Cu_2O, metallic Cu, or isolated Cu^{2+} ions incorporated into the TiO_2 lattice) and the factors that govern the Cu-doped TiO_2 photo-reactivity are still under debate. Also, there is a need to develop treatment methods that are more effective in eliminating dyes from waste streams. Ionizing radiation is known to degrade numerous pollutants. As in the case of photocatalysis, some publications reported that the addition of nanoparticles such as TiO_2 and AlO_2 in solution enhances the degradation of pollutants and accelerates the reaction induced by ionizing radiations [34-37]. However, the effect of doping on radiocatalysis has not been reported.

This work explores the local chemical environment of Cu dopants in the core and the near-surface regions of TiO_2 nanoparticles prepared by a simple sol-gel route and annealed at 400°C or 600°C. The characterization studies were conducted using various investigation techniques, including ultraviolet-visible spectroscopy (UV-vis), X-ray diffraction (XRD), transmission electron microscopy (TEM), electron energy-loss spectroscopy (EELS) and electron paramagnetic resonance (EPR) spectroscopy. Methylene blue (MB) was selected as a model compound for evaluating the potential of doped and undoped TiO_2 to remove dyes from wastewater. By investigating the effect of the copper doping level and heat treatment on

the structural and optical properties of a series of TiO_2 catalysts and subsequently on their MB degradation efficiency under gamma illumination, we show that the performance of such systems strikingly depends on the nature and distribution of the Cu species incorporated.

2. Experimental details

Pure and Cu^{2+}-doped TiO_2 powders (Cu-TiO_2) were prepared via a sol-gel technique. Details are presented in our previous work [6]. This method produces powders of high chemical purity. In this case the measured atomic ratio of Cu to Ti is between 0 and 12 at.%. Undoped TiO_2 samples were prepared as a controlin the same way. The obtained millimetric solids were ground in an agate mortar to get fine nanopowders. The nanopowders were systematically characterized after heat treatment at 400°C or 600°C in order to optimize their synthesis. In this regard, XRD, TEM and EELS are suitable characterization techniques as they allow one to identify the structures of crystallized phases and to observe possible structural changes after doping and heat treatment.

The X-ray diffractometer used was a Siemens D5005 in Bragg-Brentano geometry, furnishing CuKα radiation (λ = 1.5406 Å). The diffractograms were recorded at room temperature and the X-ray data were collected from 20° to 80° (2Θ), with a measurement time of 10 seconds and a step size of 0.02° (2Θ).

TEM (TOPCON 002B at 100 keV) was used to study the morphology and the crystallographic structure of the powders, and their possible changes after heat treatment and doping. Nanopowders were dispersed in ethanol before drop casting a very dilute suspension on a carbon-film copper grid.

The electronic structure of Cu-TiO_2 powders was investigated by means of EELS performed in two dedicated scanning transmission electron microscopes (STEM), a probe C_s-corrected Nion Ultra-STEM and a STEM-VG HB501, both equipped with a field emission source operated at 100 keV and coupled to a Gatan EELS spectrometer optically coupled to a

high-sensitivity (either nitrogen-cooled or electron amplifying) CCD camera. EELS does not only perform elemental analysis of Cu inserted into the TiO_2 structure after doping, it also provides information related to the local electronic structure of the materials (valence state of each element for example) with a high spatial resolution (down to the atomic scale).

For EPR analysis, the sample was inserted into a standard rectangular cavity in an EMX 71 X-band EPR spectrometer with 100 kHz magnetic field modulator operating at room temperature.

The optical measurements were performed by diffuse reflection over the 250 to 800 nm wavelength range. The reflection spectrum was measured using a UV-vis-near infrared spectrometer (Lambda-950) equipped with an integrating sphere.

Finally, the radiocatalytic activity of the synthesized samples was evaluated through the degradation of methylene blue (MB) in aqueous solution under gamma-ray irradiation at doses varying from 10 to 1500 Gy using the Tunisian Cobalt-60 radiation facility at a 80Gy/min dose rate [38, 39]. This dose rate was determined by alanine dosimeters irradiated by the facility and returned to Aerial for dose rate assessment.

In a typical experiment, a 10 mg/l aqueous solution of MB was mixed with the catalyst in a 100 ml glass dish to obtain a solution suspension of 2 g/l. The mixture solution was initially stirred for about 2h in the dark, to reach the adsorption equilibrium between MB and the powder catalyst surface. The MB concentration in the solution after the radiocatalysis reaction was estimated by using a UV-vis spectrophotometer (IC6400) and measuring the intensity maximum of the MB absorption peak at about 620 nm.

3. Results and discussion

3.1. Microstructural analysis

XRD was used as a first characterization step to identify the structures of the crystalline phases present in the powders and to monitor any possible structural changes upon heat

treatment and doping. The presence of a possible second phase was also looked for. **Fig. 1** shows XRD patterns of the Cu-TiO_2 samples annealed at 600°C. Importantly, we note that powders with 0-3 at.% Cu concentration are a mixture of anatase and rutile phases without any detected additional phase. The fraction of the rutile phase increases with doping levels, from 20% for undoped TiO_2 to 44% for 3at.% Cu-TiO_2. Therefore, it is clear that within this doping level range, the Cu doping promotes the anatase-to-rutile phase transition. This may be caused by the substitution of Cu^{2+} ions for Ti^{4+} ions within the anatase structural framework. Indeed, it is a well-known fact that the TiO_2 anatase structure is metastable with respect to rutile. In both rutile and anatase, Ti is six-fold coordinated, but the number of shared octahedral edges increases from two in rutile to four in anatase [40]. The tolerance of the TiO_2 structure to Cu doping can be qualitatively related to the local environment of Ti and the introduced strain. When Cu^{2+} ions enter the TiO_2 lattice, substituting for Ti^{4+} ions, the ion charges should be compensated by an increase in oxygen vacancies, that act as nucleation sites for the anatase-to-rutile transformation. At the annealing temperature of 600°C, these defects promote the transition from a metastable anatase phase to a more stable phase, more tolerant of defects, i.e. rutile. At a higher Cu doping level (6 at.%) we note the almost complete disappearance of the rutile phase and the appearance of an additional phase identified as CuO. The amount of this phase increases with Cu concentration. Once part of the Cu^{2+} ions is segregated outside the TiO_2 structure, the number of oxygen vacancies decreases, leading to the inhibition of the anatase-to-rutile transformation. Other notable changes were observed: the estimated "a (= b)" and "c" lattice parameters for undoped TiO_2 powder are respectively 3.781 Å and 9.478 Å in the anatase structure and 4.592 Å and 2.957 Å in rutile. With the increase in Cu^{2+} concentration from 0 to 3 at.%, the value of these lattice parameters hardly changes. Upon further increase of the Cu^{2+} concentration, only anatase crystallites are observed (as already mentioned), accompanied by a shift of the (101) and (200) reflections

toward larger angles. According to [9], this shift may reflect the interstitial incorporation of Cu^{2+} ions within the TiO_2 lattice. Such incorporation is promoted by an excess of copper. Interstitial doping generates stress in the anatase structure. Moreover, it does not provide additional oxygen vacancies and therefore inhibits the transition to the rutile phase. XRD measurements on pure TiO_2 and Cu-TiO_2 sol-gel powders annealed at 400°C (not shown here) exhibit only diffraction peaks corresponding to the anatase phase without any secondary phase nor any notable change in lattice parameter, within the detection limits of XRD measurements.

The average crystallite size as a function of the Cu levels for samples annealed at 400°C and 600°C **(Fig. 2)** has been evaluated from the full width at half maximum (FWHM) of the most intense peaks (the (101) and (110) peaks for anatase and rutile respectively) using the Scherrer method [41]. As previously reported [6], the crystallite size increases with annealing temperature. Moreover, it appears that Cu incorporation has a different effect on crystal growth for each temperature. For samples annealed at 400°C the crystallites are smaller than those in the undoped material, by 25% for the 3at.% Cu-TiO_2 sample, with no detectable change of lattice parameters. The crystallite size evolution according to the doping level must be related to the insertion of doping atoms in the TiO_2 structure. The substitution of metal ions of lower valence values for Ti^{4+} increases the oxygen deficiency to maintain charge neutrality. The reduction in crystallite size could be due to the formation of oxygen vacancies. In fact, defects can influence considerably the nucleation, growth, and structure of crystals [42, 43]. For samples annealed at 600°C, the opposite is observed: for a doping level not exceeding 3 at.%, doping leads to an increase in the average crystallite size (in both rutile and anatase phases). This result will be further discussed following a nano-structural study (see section 3.2). For both annealing temperatures and at a high Cu doping level (> 6 at.%) a slight decrease in the size of the crystallites (present only in the anatase phase) is observed. Such a

relative reduction in crystallite size in the presence of segregation of copper cations and/or a copper oxide additional phase at the grain boundaries has already been observed for Co-doped TiO_2 [6]. This effect seems to increase with temperature as the relative difference between the crystallite size of doped and undoped samples increases with temperature. Above 6 at.% the Cu^{2+} doping level does not show any significant effect on grain growth. Thus, we assume that at these high doping levels, the solubility limit of copper in the TiO_2 structure is exceeded and Cu^{2+} ions are segregated to the grain surfaces. We will come back to this statement in the nanoscale analysis section.

3.2. Nanoscale analysis

As the energy-loss near-edge fine structures (ELNES) are sensitive to the oxidation state and to the bonding and local environment, it is not only possible to determine the chemical composition of the doped TiO_2 samples, but also to sort out spectral signatures of the copper oxidation state and to locally identify the TiO_2 crystalline phase (anatase vs rutile) in the studied samples. Chemical analyses were performed by EELS in the spectrum-imaging mode, in which the focused beam is scanned over a region of interest and a whole spectrum is acquired at each position of the scan [44, 45]. Such a spectrum-image contains typically 10000 spectra. These spectra can be processed individually, usually by removing the background and summing the intensity corresponding to a characteristic edge and thus building elemental maps. However, as this data set contains a lot of redundant information, it is often very useful to process it as a whole using multivariate statistical techniques [46]. We used principal component analysis (PCA) as a filtering method for separating meaningful signal components from noise. In a few favorable cases, we used spectral unmixing methods. These methods assume that the whole spectrum-image can be described by a few reference spectra, each individual spectrum of the original data cube being a linear combination of these

basic components [47, 48]. We used Vertex Component Analysis [49] to perform this unmixing step.

TEM and high angle annular dark field (HAADF) STEM images of the 3at.% Cu-TiO_2 sample annealed at 400°C are displayed in **Fig. 3(a)** and **Fig. 3(b)** respectively, for two different areas in the sample. Typical samples are well crystallized and crystallites exhibit polyhedral shapes with a mean size around 10-15 nm, in agreement with XRD investigations. The inspection of the diffraction pattern confirms the anatase structure of the prepared samples with no detectable trace of the rutile phase. The Ti, O and Cu elemental maps extracted from the EELS spectra acquired in the spectrum-imaging mode are shown in **Fig. 3(c, d, e)** respectively. **Fig. 3** also shows the presence of metallic copper nanoparticles of size less than 2 nm (indicated by an arrow in **Fig. 3(b))** which are not detected by XRD. The corresponding EELS Cu $L_{2,3}$ spectrum is shown and labeled (1) in **Fig. 3(f)**. The Cu-$L_{2,3}$ spectrum from the square region, labeled (2) in **Fig. 3(e)**, displays a lower signal-to-noise ratio and characteristic features of Cu^{2+} (**Fig. 3(f)**). In fact, the Cu-$L_{2,3}$ edge shape, which reflects electronic transitions from 2p to 3d levels, is very sensitive to the oxidation state of the copper ion. The absorption edge of metallic copper Cu^0 (d10s1) exhibits a typical step like shape, while for Cu^{2+} (d9s0) most of the intensity in the near-edge region is concentrated in two narrow peaks, called L_3 and L_2 white lines. The Cu^{2+} L edge threshold is also shifted to lower energy by around 2 eV in comparison to the metallic state. It should be noted that the Cu^{1+}(d10s0) ELNES (not shown here) exhibits an increase in L_3 white line intensity in comparison to metallic copper, but no chemical shift [50].

Fig. 4(a) shows a higher magnification TEM image together with its corresponding selected area electron diffraction (SAED) pattern of 6at.% Cu-TiO_2 annealed at 400°C. The SAED pattern confirms the anatase structure of these polycrystalline powders [6]. We also note the presence of grain boundaries. Elemental maps as extracted from EELS spectrum-

images of the region of interest associated with the HAADF image displayed in **Fig. 4(b)**, are shown in **Fig. 4(c, d)** for the energy regions including the Ti-$L_{2,3}$ and Cu-$L_{2,3}$ edges respectively. These elemental maps show the presence of copper-rich nanoparticles (1-2 nm in diameter) at grain surfaces and a copper segregation at the grain boundaries. These secondary phases were not detected by XRD. In **Fig. 4(e)** we have manually applied two thresholds to the Cu map in order to separate the particles (visible in red) from the grain boundaries (in green). The spectra summed over the corresponding pixels are shown in **Fig. 4(f)**. It appears that the grain boundaries contain mostly oxidized Cu^{2+} as indicated by the strong intensity in the white lines. The EELS fine structures corresponding to the particles exhibit a much-reduced white line intensity due to a strong contribution of a metallic Cu signal. From doping levels of about 3 at.%, the TiO_2 structure begins to be saturated with Cu. The electrons trapped in oxygen vacancies (whose presence assures electron neutrality of the sample upon Ti^{4+} substitution) may be transferred to the Cu^{2+} ions segregated on the crystallite surface, resulting in metallic Cu formation.

Results from a nanoscale analysis of Cu-TiO_2 samples annealed at 600°C are summarized in **Fig. 5**. For samples with a Cu concentration of 3 at.%, the typical crystallite morphology is shown in the HAADF images of **Fig. 5(a)** and **Fig. 5(d)**. Large TiO_2 particles with faceted shapes are observed. The mean particle size is found to be around 55 nm (in agreement with XRD analysis). The Cu map (Cu-$L_{2,3}$ edge intensity map) of **Fig. 5(b)** clearly shows a copper segregation at the TiO_2 crystallite surface and grain boundaries. As in the case of the 400°C annealed sample, we have applied a thresholding to the Cu map in order to separate the signal coming from the larger metallic copper particles (in red) from that of a weaker segregation at surfaces and grain boundaries (in green). Cu-$L_{2.3}$ edges thus obtained are presented in **Fig. 5(c)** and show slightly different oxidation states. In a few cases a strong copper segregation is observed at grain boundaries allowing for the signal extraction by

statistical analysis of this secondary phase. Maps obtained after spectral unmixing of sets of spectra encompassing the Ti-$L_{2,3}$ to O-K energy region are presented in **Fig. 5(e**). These maps show the presence of both anatase and rutile phases (blue and green pixels in the image of **Fig. 5(e)**). A third component is extracted, which is characteristic of the grain boundaries (red pixels). The EELS components corresponding to these maps are presented in **Fig. 5(f)**. It is clearly possible to distinguish a rutile grain (in green) from the surrounding anatase ones (in blue)**. Fig. 5(g)** and **Fig. 5(h)** show the result of a second VCA treatment applied when considering a larger energy range encompassing the Ti-$L_{2,3}$, O-K and Cu-$L_{2,3}$ edges. The map associated with the VCA component related to Cu segregation at grain boundaries is shown in **Fig. 5(g)**. The associated Cu-$L_{2,3}$ edge after background subtraction is shown in **Fig. 5(h).** The edge fine structures clearly indicate that the copper segregation at the grain boundaries involves a high copper oxidation state (Cu^{2+}). An elemental quantification of this VCA EELS component gives an estimated doping level of about 3 at.% Cu. This is much more than the measured Cu content within the grains, which is well below 1 at.%. The remaining copper is probably present in an undetected additional phase.

The Ti-$L_{2.3}$ ELNES corresponding to 3at.% Cu-TiO_2 samples annealed at 400°C and 600°C are presented in **Fig. 6(a).** All are composed of two main contributions, namely the L_3 and L_2 edges, separated by the 2p core-hole spin–orbit coupling. The L_3 and L_2 edges are then both subdivided into two peaks by the strong crystal field splitting created by the surrounding oxygen atoms [51-54]. All the spectra have a similar form and are consistent with the TiO_2 anatase structure for samples annealed at 400°C and with both anatase and rutile structures for samples annealed at 600°C. A splitting reduction of the Ti-L_3-e_g edge induced by Cu^{2+} incorporation is observed for both anatase and rutile structures. **Fig. 6(b)** shows EELS O-K edges for undoped and 3at.% Cu-TiO_2 annealed at 400°C and 600°C. The spectra match well with the anatase and rutile TiO_2 structures. They can be decomposed in two main

spectroscopic regions labeled as (1) and (2). The pre-edge (1) results from hybridization of the oxygen 2p with the titanium 3d orbitals. A stronger crystal field splitting is observed for rutile than anatase (associated with a 2.75 eV and 2.5 eV t_{2g}-e_g splitting respectively) [55]. (2) corresponds to electron transitions from 1s to 2p oxygen states hybridized with titanium 4s and 4p states that are sensitive to long-range connectivity changes between oxygen octahedra in the TiO_2 structure. For all doped samples, the spectra of **Fig. 6** show that the Ti-$L_{2,3}$ and O-K ELNES modifications due to the structural distortion induced by Cu^{2+} substitution are more marked at the grain boundaries, but are also present within the bulk of the TiO_2 crystallites. Importantly, according to the recorded ELNES, we can rule out the presence of significant quantities of Ti^{3+} in all studied samples.

We now come back to the previous discussion on the particle size. For samples annealed at 400°C, the average crystallite size decreases by 25% when the Cu content increases from 0 to 3 at.%. The opposite is seen for samples annealed at 600°C: a strong increase of about 50% and 30% of the crystallite size, respectively in anatase and rutile phases is observed. Nanoscale investigation reveals that the TiO_2 structure annealed at 600°C has a lower Cu saturation limit. Therefore, the true Cu doping concentration in the TiO_2 lattice annealed at 600 °C is lower than that in samples annealed at 400°C. Any size reduction due to growth inhibition in the presence of oxygen vacancies created by Cu^{2+} substitution is thus expected to be much more limited. However, oxygen vacancies and their effect on crystal growth cannot explain the crystallite size evolution discrepancy between both annealing temperatures.

In fact, the growth of such small nanoparticles is probably more dominated by surface processes than bulk ones. We speculate that the growth mechanism during annealing is affected by the presence of copper at the surface. For example, it has been suggested by Wu et al. for Fe-doped TiO_2 samples that the presence of Fe^{3+} ions at the surface decreases the free

energy and thereby reduces the thermodynamic driving energy of particle growth [56]. Alternatively, other mechanisms such as sintering [57] may be at the origin of an increase of particle size in the presence of copper.

3.3. Electron paramagnetic resonance (EPR) study

EPR spectroscopy analyses were performed in order to monitor the involved paramagnetic centers and to follow the valence state and the coordination environment of the doping ions as a function of Cu doping concentration in the TiO_2 lattice. The evolution of the EPR signal of undoped and copper-doped TiO_2 samples, annealed at 400°C, are shown in **Fig. 7**. The sharp peak observed at g = 2.003 closely approaches the free electron *g* value (*g* = 2.002). This value is associated with single electrons trapped in oxygen vacancies from the TiO_2 lattice [58]. Undoped samples have only this paramagnetic signal. For a doping level not exceeding 0.3 at.% of Cu^{2+} the intensity of this EPR peak increases and an asymmetric EPR signal shape appears whose intensity also increases. This EPR signal corresponds to the presence of Cu^{2+} (3d9) ions in octahedral coordination in the TiO_2 lattice. This result is in agreement with that obtained by B. Choudhry et al. [11], confirming the substitution role of Cu^{2+} ions in the TiO_2 network. The substitution of Cu^{2+} for Ti^{4+} ions in the TiO_2 lattice leads to the formation of oxygen vacancies. It has been disclosed that for anatase the doping with a cation, such as Cu^{2+}, Co^{2+}, Fe^{3+}, with a lower valence than that of the Ti^{4+} ion, introduces oxygen vacancies inhibiting the formation of Ti^{3+} ions [11, 15, 6, 56]. We also note that these oxygen vacancy sites are electron traps [59, 60]. Following the Cu^{2+} doping, the place occupied by the O^{2-} anion in the regular TiO_2 lattice is taken by one or two free electrons, thus forming a donor level below the conduction band. It is demonstrated that these donor states in both anatase and rutile increase with increasing oxygen vacancies and can overlap the conduction band [61]. This may explain the great decrease in the band gap of TiO_2 produced by Cu^{2+} doping.

At a higher doping level (0.6at.% Cu-TiO_2) a decrease in oxygen vacancy sites is noted, which is accompanied by an increase in the peak-to-peak height (PPH) of the Cu^{2+} ion spectral signature (**Fig. 7(b)**). This may be due to the insertion of Cu^{2+} ions in the interstitial sites in addition to substitution. At doping levels up to 3 at.%, the decrease in the oxygen vacancies PPH is more pronounced and is accompanied by a decrease in the Cu^{2+} ion signal PPH. The Cu^{2+} ion EPR signal also broadens, suggesting that a dipolar interaction among neighboring Cu^{2+}ions is taking place. The nanoscale investigation in section 3.2 reveals the presence of metallic copper nanoparticles in the grain boundaries at and above a 3 at.% copper doping level. The electrons trapped inTiO_2 oxygen vacancies can be transferred to the Cu^{2+} ions and metallic Cu is thus formed. This charge transfer can explain the decrease in the Cu^{2+} EPR signal PPH.

3.4. Optical properties

The optical properties of Cu-TiO_2 powders annealed at 400°C and 600°C were investigated by UV-vis spectroscopy in diffuse reflectance mode (DRS). The reflectance data R% was converted to the Kubelka-Munk function F(R) by the equation: $F(R) = \frac{(1-R)^2}{2R}$ which is proportional to the absorption coefficient $\propto$. The optical gap value is estimated using the Kubelka-Munk method combined with the Tauc relation [62]: $\propto h\nu = A(h\nu - E_g)^{m}$, where $h\nu$ is the photon energy, A is an energy dependent constant and m an integer depending on the nature of the electronic transitions. For an indirect transition m = 2 and for a direct one m = 1/2. By plotting $(F(R).h\nu)^{\frac{1}{2}}$ as a function of energy excitation, we estimate the indirect energy band gap E_g^I and likewise $(F(R).h\nu)^2$ to estimate the direct band gap energy E_g^d. According to theoretical investigations, the substitution of Cu^{2+} for Ti^{4+} in anatase (2at.% Cu-doped TiO_2) should lead to a decrease in the band gap, down to 1.7 eV, and an increase in the visible light absorption [15, 21]. Indeed, as already mentioned, Cu^{2+} substitution in TiO_2 is accompanied by the formation of oxygen vacancies to preserve electric neutrality. In a

simplistic ionic model, along with Cu^{2+} acceptor defect states, oxygen donor band states are formed in the band gap [21]. Using more sophisticated models, the appearance of new states at the top of the valence band and the bottom of the conduction band after Cu^{2+} doping has been shown to result from the strong iono-covalency of the Cu-O bonding which has a strong O2p-Cu3d hybridized character [15]. The absorbance spectra corresponding to the Kubelka-Munk function versus wavelength and the band gap energy estimations for Cu-TiO_2 powders annealed at 400°C and 600°C are represented in **Fig. 8.** As expected, the insets in **Fig. 8(a)** and **Fig. 8(b)** show a general red shift in the UV-visible absorption spectra as a function of the Cu concentration. Undoped TiO_2 exhibits strong absorption in the UV region and high transparency in the visible. Copper incorporation into the TiO_2 lattice leads to a general shift in the UV-visible absorption spectra and to the creation of an increasingly (with Cu content) strong broad absorption band in the visible range. Two typical effects are observed: (i) the appearance of an absorption band between 400 and 500 nm that could be caused by the hybridization between O2p from TiO_2 and Cu^{2+} 3d states [4, 11, 15, 21]. This band has been shown also to appear due to charge transfer between TiO_2 and CuO clusters [63] at the TiO_2/CuO interface. The possible presence of metallic copper can also affect the absorbance of this material in the visible range, via plasmonic excitations. (ii) the appearance of abroad absorption band between 600 and 900 nm, which is not observed in pure TiO_2, and which is attributed to d-d transitions between the newly created energy levels at the top and bottom of the valence and conduction bands when Cu^{2+} is inserted into the TiO_2 crystalline environment [11, 15]. This typical behavior and these types of electronic transitions are consistent with those observed in the literature [11, 12] and indicate once more the substitution of Ti^{4+} by Cu^{2+}. Resulting indirect (E_g^I) and direct (E_g^d) energy band gaps were estimated graphically in a first approximation via the Tauc relation [62] by extrapolation of the Tauc plot to the hν axis with a linear fit. The obtained values are shown in **Fig. 8(c)**. In the TiO_2 energy band

structure, the top of the valence band originates mainly from O_{2p} states and the conduction band from Ti_{3d} states. The presence of the extra element in the TiO_2 lattice leads to a decrease of both direct and indirect band gaps. However, the most significant decrease is recorded for the indirect gap. For undoped samples, the band gap decreased slightly with increasing annealing temperature. This is in agreement with an increase in the rutile fraction with temperature. The presence of Cu^{2+} ions in the TiO_2 structure has an even stronger effect on the band gap value reduction. In fact, we note that, at doping levels greater than 0.6 at.%, samples annealed at 400 °C present the largest band gap reductions, peaking for the sample with 3 at.% of copper (1.5eV). For Cu-TiO_2 samples annealed at 400°C, when passing from a copper incorporation level of 3 at.% to 6 at.% the intensity of the 400-500 nm absorption band increases while the 600-900 nm absorption band decreases (**Fig. 8(a)**). This suggests that the effective copper doping level in the 6at.% Cu-TiO_2 samples is lower than in 3at.% Cu-TiO_2. Indeed, at higher copper incorporation levels, microanalysis investigations confirm the segregation of copper oxide species at the surface of the crystallites.

For Cu-TiO_2 samples annealed at 600°C the incorporation of Cu^{2+} into the TiO_2 structure also enhances the absorption by the catalyst in the visible range and induces a shift in the band gap to lower energies, though less pronounced than at 400°C. According to the structural investigations, this finding can be attributed to the absorption caused by: (i) metallic copper clusters formed in grain boundaries, and (ii) the disordered, highly Cu-doped TiO_2 structure formed in the grain boundaries. These interpretations concern samples with doping level no greater than 3 at.% of copper. The band gap decreases from 3.04 to 2.06 eV and 1.98 eV for a doping level of 6 at.% and 12 at.% respectively. These variations are probably due to the presence of the CuO additional phase, which presents a gap of around 1.5eV. As shown in **Fig. 8(b)**, the contribution of this extra phase becomes rather large, which makes difficult the estimation of the gap through the methods used here on the diffuse reflectivity data.

3.5. Radiocatalytic activity evolution

Fig. 9 shows the effects of radiolytic and radiocatalytic degradation of methylene blue (MB) as a function of gamma-ray doses. **Fig. 9(a)** shows the radiocatalytic degradation curves of MB as a function of dose for different Cu dopant content in Cu-TiO_2 catalysts calcined at 400°C for 6 h. It is found that the degradation ratio of MB increases gradually with gamma dose. Under gamma irradiation and without any TiO_2 catalyst, MB presents a similar degradation to that reported previously in the literature [64]. We then find that the insertion of copper into the TiO_2 structure is beneficial to the radiocatalytic efficiency. In the presence of Cu-TiO_2 catalyst the MB degradation is about 25% higher than for undoped TiO_2. At low gamma radiation doses ($\leq$ 100 Gy) the best degradation was obtained with 3at.% Cu-TiO_2. The presence of more copper in the TiO_2 structure becomes slightly beneficial to the radiocatalytic activity only for high gamma radiation doses ($\geq$ 500 Gy). The best radiocatalytic performance obtained for a 3at.% Cu-TiO_2 catalyst annealed at 400°C is probably due to the large reactive surface area and the low band gap energy values. As revealed by XRD measurements, at this doping level the produced samples have the smallest particle size and possibly have the highest specific surface area. In fact, as reported by many authors, e.g., [9], the specific surface area increases in inverse proportion to the sol-gel TiO_2 particle size. Our structural and optical results revealed that Cu^{2+} internal doping of the TiO_2 structure occurs and leads to a very low band gap. During the radiocatalytic process, gamma irradiation can also lead to the desorption of oxygen from the crystallite surface. The oxygen vacancies so created can form donor levels in the TiO_2 forbidden band gap and can also act as traps for photogenerated electrons, thereby limiting the electron-hole recombination. With further copper doping level increases, CuO partially covers the surface of the TiO_2 catalyst. CuO/TiO_2 heterostructures thus formed can facilitate the carrier separation and lead to improved radiocatalytic properties.

Regarding the second set of Cu-TiO_2 samples annealed at 600°C, the degradation rate as a function of gamma-ray dose is presented in **Fig. 9(b)**. Pure TiO_2 synthesized at 600℃ presents better radiocatalytic performance than at 400℃, even though for TiO_2 catalysts it is generally accepted that anatase exhibits a higher photocatalytic activity than rutile [65]. Indeed, anatase is an indirect band gap semiconductor in contrast to rutile. This leads to a longer lifetime for photogenerated electrons and holes in anatase than in rutile. However, an optimal amount (not exceeding 20 %) of the rutile phase can result in enhanced catalytic properties. This synergistic effect (like that observed in commercial TiO_2 powders, Degussa P25) is controlled by the band alignment between rutile and anatase, which is favorable to charge separation (see [66] for more details). Higher rutile percentages will generate trap sites for carrier recombination.

We observe at this temperature that Cu doping leads to a decrease in the radiocatalytic activity of the TiO_2 catalyst. At this annealing temperature samples present a much lower specific surface than undoped ones (crystallites are about 45% larger after doping) and are densely covered with copper species, inhibiting the catalytic properties of TiO_2. For samples doped with 3 at.% of copper, structural investigations show an increase in the proportion of rutile (about 44%). For higher doping levels, the specific surfaces are even smaller, but the return to a pure anatase phase can explain the slight increase in the MB catalytic degradation efficiency as compared to that obtained with 3at.% Cu-TiO_2 catalysts.

In summary, the best catalytic performance under gamma radiation was observed for copper-doped TiO_2 samples annealed at 400°C, copper being inserted in substitutional sites of the anatase structure. These samples have a high specific surface area and a small band gap. We note that during radiocatalysis, high-energy radiation is known to generate oxygen vacancies at the catalyst surface [67-69] that act as electron traps [61]. Such defects have been reported to affect surface adsorption of H_2O and O_2 on TiO_2 and to promote H_2O dissociation

[70] and formation of hydroxyl groups, therefore accelerating the organic pollutant degradation process.

4. Conclusions

This work investigates a novel approach for destroying organic pollutants involving transition-metal-doped titania. Amongst the advantages of using ionizing radiation is the fact that it overcomes optical transparency limitations associated with visible and near-UV illumination. The performance of such systems depends strongly on the insertion of impurities in the TiO_2 structure and their resulting distribution. We have shown that 3at.% Cu-TiO_2 catalysts annealed at 400°C present very small crystallites and therefore the highest specific surface, the most reduced band gap, due to Cu^{2+} insertion in the TiO_2 lattice and so the best radiocatalytic performance. We suggest that oxygen vacancies generated during the radiocatalytic process form donor levels in the forbidden band gap of TiO_2 and can also act as traps for the photogenerated electrons thereby limiting the electron-hole recombination. We also suggest that at higher annealing temperature, the much lower specific surface and the copper species present on the surfaces and at grain boundaries inhibit the radioacatalytic performances.

References

[1] M. A Henderson. A surface science perspective on TiO_2photocatalysis, Surf. Sci. Rep. 66 (2011) 185-278.

[2] P. Pichat, Fundamentals of TiO_2 Photocatalysis. Consequences for Some Environmental Applications. Heterogeneous Photocatalysis, Part of the series Green Chemistry and Sustainable Technology, Springer, 2015, pp. 321-359.

[3] B. Su, J. Xin, J. Li, T. Zheng, Q. Wang, Z. Lei, The role of multi-level structure for the improved photocatalytic performance of TiO_2 fiber nanomaterial, Appl. Phys. A. 122 (2016) 32-39.

[4] G. Colon, M. Maicu, M.C. Hidalgo, J.A. Navıo, Cu-doped TiO_2 systems with improved photocatalytic activity, Appl. Catal. B Environ. 67 (2006) 41-51.

[5] J. Pan, S. P. Jiang. Synthesis of nitrogen doped faceted titanium dioxide in pure brookite phase with enhanced visible light photoactivity, J. Colloid Interface Sci. 469 (2016) 25-30.

[6] L. Samet, J. Bennasseur, R. Chtourou, K. March, O. Stephan, Heat treatment effect on the physical properties of cobalt doped TiO_2 sol-gel materials, Mater. Charact. 85 (2013) 1-12.

[7] X. H. Xia, L. Lu, A. S.Walton, M.Ward, X. P.Han, R.Brydson, J. K. Luo, G. Shao, Origin of significant visible-light absorption properties of Mn-doped TiO_2 thin films, Acta Mater. 60 (2012) 1974-1985.

[8] W. P. Hudson, M. V. J. R. Carvalho, P. Hammer, C. R.Teodorico, TiO_2-Cu photocatalysts: a study on the long- and short-range chemical environment of the dopant, J. Mater. Sci.48 (2013) 3904-3912.

[9] T. Aguilar, J. Navas, R. Alcántara, C. Fernández-Lorenzo, J. J. Gallardo, G. Blanco, J. Martín-Calleja, A route for the synthesis of Cu-doped TiO_2 nanoparticles with a very low band gap, Chem. Phys. Lett. 571 (2013) 49-53.

[10] I. Ganesh, P. P. Kumar, I. Annapoorna, J.M. Sumliner, M. Ramakrishna, N.Y. Hebalkar, G. Padmanabham, G. Sundararajan, Preparation and characterization of Cu-doped TiO_2 materials for electrochemical, and photocatalytic applications, Appl. Surf. Sci. 293 (2014) 229-247.

[11] B. Choudhury, M. Dey, A. Choudhury, Defect generation, d-d transition, and band gap reduction in Cu-doped TiO_2 nanoparticles, Int. Nano Lett. 3 (2013) 25-33.

[12] C. Karunakaran, G. Abiramasundari, P. Gomathisankar, G. Manikandan, V. Anandi, Cu-doped TiO_2 nanoparticles for photocatalytic disinfection of bacteria under visible light, J. Colloid Interface Sci. 352 (2010) 68-74.

[13] O. Zuas, H. Budiman, Synthesis of nanostructured Copper-doped titania and its properties, Nano-Micro Lett. 5 (2013) 26-33.

[14] Q. Hu, J. Huang, G. Li, Y. Jiang, H. Lan, W. Guo,Y. Cao, Origin of the improved photocatalytic activity of Cu incorporated TiO_2 for hydrogen generation from water, Appl. Surf. Sci. 382 (2016) 170-177.

[15] J. Navas, A.S. Coronilla, T. Aguilar, N.C. Hernandez, D. Santos, J.S. Marquez, D. Zorrilla,C.F. Lorenzo, R. Alcantara, J.M.Calleja, Experimental and theoretical study of the electronic properties of Cu-doped anatase TiO_2, Phys. Chem. Chem. Phys. 16 (2014) 3835-3845.

[16] M. C. Wu, P.Y. Wu, T. H. Lin, T. F. Lin. Photocatalytic performance of Cu-doped TiO_2 nanofibers treated by the hydrothermal synthesis and air-thermal treatment, Appl. Surf. Sci. 430 (2018) 390-398.

[17] R. Yin, L. Ling, Y. Xiang, Y. Yang, A. D. Bokare, C. Shang. Enhanced photocatalytic reduction of chromium (VI) by Cu-doped TiO_2 under UV-A irradiation. Sep. Purif. Technol. 190 (2018) 53-59.

[18] J. Vargas, S. Coste, A. Garcia-Murillo, F. Carillo, A. Kassiba, Effects of metal doping (Cu, Ag, Eu) on the electronic and optical behavior of nanostructured TiO_2, J. Alloys Compd. 710 (2017) 355-363.

[19] W. Chakhari, J. Ben Naceur, S. Ben Taieb, I. Ben Assaker, R. Chtourou, Fe-doped TiO_2 nanorods with enhanced electrochemical properties as efficient photoanode materials, J. Alloys Compd. 708 (2017) 862-870.

[20] H. C. Huang, C. L. Yang, M. S. Wang, X. G. Ma. Enhanced photocatalytic performance of anatase TiO_2 substitutionally co-doped with La and N, Sol. Energy Mater. Sol. Cells. 170 (2017) 233-238.

[21] A. Dashora, N. Patel, D.C. Kothari, B.L. Ahuja, A. Miotello, Formation of an intermediateband in the energy gap of TiO_2 by Cu-N-codoping: first principles study and experimental evidence, Sol. Energy Mater. Sol. Cells.125 (2014) 120-126.

[22] W. Fang, M. Xing, J. Zhang. Modifications on reduced titanium dioxide photocatalysts: A review, J. Photochem. Photobiol. C. 32 (2017) 21–39.

[23] M.G. Méndez-Medrano, E. Kowalska, A. Lehoux, A. Herissan, B. Ohtani, D. Bahena, V. Briois, C. Colbeau-Justin, J.L. Rodríguez-López, H. Remita. Surface modification of TiO_2 with Ag nanoparticles and CuO nanoclusters for Application in Photocatalysis. J. Phys. Chem. C. 120 (2016) 5143–5154.

[24] Q. Wang, Q. Yuan, Z. Liu, R. Jin, Y. Cui, S. Gao. Ultrasound-assisted synthesis and solar-light-driven photoelectrocatalytic activity of CdS sensitized TiO_2 nanotube array photocatalysts, Sep. Purif. Technol. 194 (2018) 216–221.

[25] M. Yang, L. Zhang, B. Jin, L. Huang, Y. Gan, Enhanced photoelectrochemical properties and water splitting activity of self-ordered MoO_3-TiO_2 nanotubes, Appl. Surf. Sci. 364 (2016) 410-415.

[26] X. Wang,Y. Zhao , K. Mølhave, H. Sun. Engineering the Surface/Interface Structures of Titanium Dioxide Micro and Nano Architectures towards Environmental and Electrochemical Applications, Nanomaterials. 7 (2017) 1-30.

[27] R. Long, N. J. English, New Insights into the band gap narrowing of (N, P)-codoped TiO_2 from hybrid density functional theory calculations, ChemPhysChem. 12 (2011) 2604-2608.

[28] R. Long, N. J. English, Electronic structure of cation-codoped TiO_2 for visible-light photocatalysts applications from hybrid density functional theory calculations, Appl. Phys. Lett. 98 (2011)142103-142105.

[29] M. Logar, I. Bracko, A. Potocnik, B. Jancar, Cu and CuO/Titanate nanobelt based network assemblies for enhanced visible light photocatalysis, Langmuir. 30 (2014) 4852-4862.

[30] Z. J. Li, Y. Qu, G. W. He, M. Humayun, S. Y Chen, L.Q. Jing, Enhanced visible-light activities for PEC water reduction of CuO nanoplates by coupling with anatase $TiO_2$and mechanism, Appl. Surf.Sci. 351 (2015) 681-685.

[31] Q. Huang, F. Kang, H. Liu, Q. Li, X.D. Xiao, Highly aligned $Cu_2O/CuO/TiO_2$ core/shell nanowire arrays as photocathodes for water photoelectrolysis, J. Mater. Chem. A. (2013) 2418-2425.

[32] Q. Hu, J. Huang, G. Li, J. Chen, Z. Zhang, Z. Deng, Y. Jiang, W. Guo, Y. Cao, Effective water splitting using CuO_x/TiO_2 composite films: Role of Cu species and content in hydrogen generation, Appl. Surf. Sci. 369 (2016) 201-206 .

[33] N.L. Wu, M.S. Lee, Enhanced TiO_2 photocatalysis by Cu in hydrogen production from aqueous methanol solution, Int. J. Hydrogen Energy. 29 (2004) 1601-1605.

[34] P. G. Hoertz, D. Magnus-Aryitey, V. Gupta, C. Norton, S. Doorn,T. Ennis. Photocatalytic and radiocatalytic nanomaterials for the degradation of organic species, Radiat. Phys. Chem. 84 (2013) 51-58.

[35] A. Cecal, M. Goanta, M. Palamaru, T. Stoicescu, K. Popa, A. Paraschivescu, V. Anita, Use of some oxides in radiolytical decomposition of water, Radiat. Phys. Chem. 62 (2001) 333-336.

[36] F. Follut, N. Karpel Vel Leitner, Radiolysis of aquous 4-nitrophenol solution with Al_2O_3 or TiO_2 nanoprticules,Chemosphere. 66 (2007) 2114-2119.

[37] J.C. Gonzalez-Juarez, J. Jimenez-Becerril, Gamma radiation induced catalytic degradation of 4-chlorophenol using SiO_2, TiO_2 and Al_2O_3, Radiat. Phys. Chem.75 (2006) 768-772.

[38] F. Hosni, K. Farah, H. Kaouach, A. Louati, R. Chtourou, A.H. Hamzaoui, Effect of gamma-irradiation on the Colorimetric properties of epoxy-resin films: potential use in dosimetric application, Nucl. Instrum. Methods Phys. Res., Sect. B. 311 (2013) 1-4.

[39] F. Hosni, K. Farah, A. Mejri, A. Khayat, R.Chtourou, A. H. Hamzaoui, Dosimeter P. A study of the fractionation dose on the radiation response of Harwell Red-Perspex PMMA dosimeter, Nucl. Instrum. Methods Phys. Res., Sect. B. 290 (2012) 69 -71.

[40] J. Arbiol, J. Cerda, G. Dezanneau, A. Cirera, F. Peiro, A. Cornet, J. R. Morante, Effects of Nb doping on the TiO_2 anatase-to-rutile phase transition, J. Appl. Phys. 92 (2002) 853-862.

[41] E. W. Nuffield, X-ray diffraction methods.,Wiley, New York,1966.

[42] V. W. A. De Villeneuve, R. P. Dullens, D. G. A. L. Aarts, , E. Groeneveld, J. H. Scherff, W.K. Kegel, H.N.W. Lekkerkerker, Colloidal Hard-Sphere Crystal Growth Frustrated by Large Spherical Impurities, Science. 309 (2005) 1231-1233.

[43] N. Kubota, Effect of Impurities on the Growth Kinetics of Crystals, Cryst. Res. Technol. 36 (2001) 749-769.

[44] C. Jeanguillaume & C. Colliex, Spectrum-image: the next step in EELS digital acquisition and processing, Ultramicroscopy.198928 (1989) 252-257.

[45] A. Gloter, V. Badjeck, L. Bocher, N. Brun, K. March, M. Marinova, M. Tencé, M. Walls, A. Zobelli, O. Stéphan, C. Colliex, Atomically resolved mapping of EELS fine structures, Mater. Sci. Semicond. Process. 65 (2017) 2-17.

[46] F. De La Peña, M. H. Berger, J. F. Hochepied, F. Dynys, O. Stephan, M. Walls, Mapping titanium and tin oxide phases using EELS: An application of independent component analysis, Ultramicroscopy.111 (2011) 169-176.

[47] N. Dobigeon, N. Brun, Blind Linear unmixing of EELS spectrum-images, Ultramicroscopy. 120 (2012) 25-34.

[48] N. Dobigeon, Y. Altmann, N. Brun, S. Moussaoui, Linear and non linearunmixing in hyperspectral imaging, in Resolving spectral mixtures - With application from ultrafast time-resolved spectroscopy to super resolution imaging, C. Ruckebusch,Data Handling in Science and Technology Series. 30, Ed. Oxford., U.K.: Elsevier. 30, 2016 pp. 185-224.

[49] J. M. P. Nascimento, J. M. Bioucas-Dias, Vertex component analysis: A fast algorithm to unmix hyperspectral data, IEEE Trans. Geosci. Remote Sens. 43(4) (2005) 898-910.

[50] M. Backahaus-Ricoult, L. Samet, M.F. Trichet, M.J. Hytch, D. Imhoff, Interfacial chemistry in internally oxidized (Cu, Mg)-alloys, J. Solid State Chem. 173 (2003) 172-188.

[51] R. Brydson, H. Sauer, W. Engel, J. M.Thomas, E. Zeitler, N. Kosugill, H. Kurodall, Electron energy loss and x-ray absorption spectroscopy of rutile and anatase: a test of structural sensitivity, J. Phys.: Condens. Matter. 1 (1989) 797-812.

[52] J. P. Corombette, F. Jollet, Ti2p X-ray absorption in tianium dioxides (TiO_2): the influence of the cation site environment, J. Phys.: Condens. Matter. 6 (1994) 10811-10821.

[53] G. S. Henderson, X. Liu, M. E. Fleet, A Ti-L edge X Ray absorption study of Ti-silicate glasses, Phys. Chem. Miner. 29 (2002) 32-42.

[54] G. Bertoni, E. Beyers, J. Verbeeck, M. Mertens, P. Cool, E.F. Vansant, G. Van Tendeloo, Quantification of crystallineand amorphous content in porous TiO_2 samples from electron energy loss spectroscopy, Ultramicroscopy. 106 (2006) 630-635.

[55] A. Gloter, C. Ewels, P. Umek, D. Arcon, C. Colliex, Electronic structure of titania-based nanotubes investigated by EELS spectroscopy, Phys. Rev. B: Condens. Matter Mater. Phys. 80 (2009) 035413-035419.

[56] Q. Wu, Q. Zheng, R. Van de Krol, Creating Oxygen Vacancies as a Novel Strategy To Form Tetrahedrally Coordinated Ti^{4+} in Fe/TiO_2 Nanoparticles, J. Phys. Chem. C. 116 (2012) 7219-7226.

[57] W. Tuichai, S. Danwittayakul, N. Chanlek , P. Thongbai, Effects of sintering temperature on microstructure and giant dielectric properties of (V + Ta) co-doped TiO_2 ceramics, J. Alloys Compd.725 (2017) 310-317.

[58] Y. Sun, T. Egawa, L. Zhang, X. Yao, Novel method to directly prepare high-surface-area anatase titania nanoparticles with trapped electrons on oxygen vacancies, J. Mater. Sci. Lett. 22 (2003) 799-802.

[59] H. Li, Y. Guo, J. Robertson, Calculation of TiO_2 Surface and Subsurface Oxygen Vacancy by the Screened Exchange Functional, J. Phys. Chem. C. 119 (2015) 18160-18166.

[60] C. Papageorgiou Anthoula, S. Beglitis Nikolaos, L. Pang Chi, G. Teobaldi,C. Gregory, Q. Chen, J. Fisher Andrew, A. Hofer Werner, G. Thornton, Electron traps and their effect on the surface chemistry of TiO_2 (110), PNAS. 107 (2010) 2391-2396.

[61] X. Pan, M. Q. Yang, X. Fu, N. Zhang, Y. Xu, Defective TiO_2 with oxygen vacancies: synthesis, properties and photocatalytic applications, Nanoscale. 5 (2013) 3601-3614.

[62] S. Tandon, J. Gupta, Measurement of forbidden energy gap of semiconductor by diffuse reflectance technique, Phys. Status Solidi B. 38 (1970) 363-367.

[63] G. Li, N. M. Dimitrijevic, L. Chen, T. Rajh, Role of surface/interfacial Cu^{2+} sites in the photocatalytic activity of coupled CuO-TiO_2 nanocomposites, J. Phys. Chem. C. 112 (2008) 19040-19044.

[64] B. Zheng, C. Li, L. Jiang, L. Lizheng Liang, W. Pen , J. Niu, Degradation of Methylene Blue in aqueous solution by gamma irradiation, The 5 th International Conference on Bioinformatics and Biomedical Engineering (IEEE). (2011) 1-4.

[65] J. Zhang, P. Zhou, J. Liu, J. Yu, New understanding of the difference of photocatalytic activity among anatase, rutile and brookite TiO_2, Phys. Chem. Chem. Phys. 16 (2014) 20382-20386.

[66] Y. Mi, Y. Weng, Band alignement and contrillable elecron migration between rutile and anatase TiO_2, Sci. Rep. 11482 (2015) 1-10.

[67] L.-Q. Wang, D. R. Baer, M. H. Engelhard, A. N. Shultz, The adsorption of liquid and vapor water on TiO_2(110) surfaces: the role of defects, Surf. Sci. 344 (1995) 237-250.

[68] S. Eriksen and R. G. Egdell, Electronic excitations at oxygen deficient TiO_2 (110) surfaces: A study by EELS, Surf. Sci. 180 (1987) 263-27.

[69] M. L. Knotek, P. J. Feibelman, Ion Desorption by Core-Hole Auger Decay, Phys. Rev. Lett. 40 (1978) 964-967.

[70] R. Schaub, P. Thostrup, N. Lopez, E. Lægsgaard, I. Stensgaard, J. K. Nørskov and F. Besenbacher, Oxygen Vacancies as Active Sites for Water Dissociation on Rutile TiO_2 (110), Phys. Rev. Lett. 87 (2001) 266104-266108.

Graphical Abstract (for review)

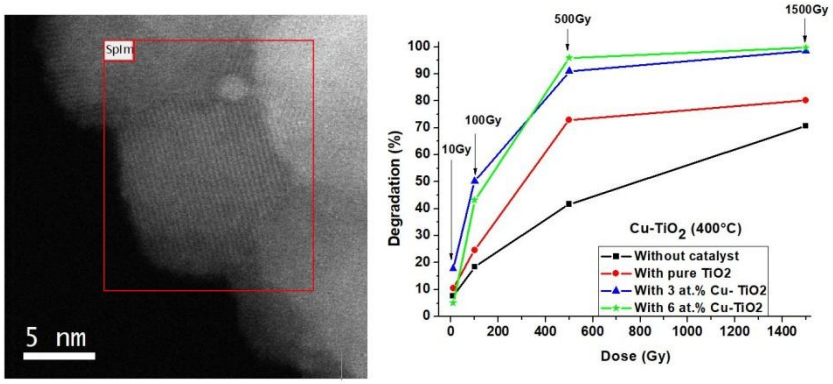

Highlights :

- ✓ Copper doped and undoped TiO_2 powders were prepared by sol-gel route.
- ✓ Nanoscale analysis show evidence of internal doping by Cu^{2+} in the TiO_2 sublattice.
- ✓ Substitution reduce the optical band gap down to 1.5 eV.
- ✓ Metallic copper segregation is formed at the crystallite surfaces.
- ✓ Anatase Cu doped TiO_2 improves significantly the radiocatalytic efficiency.

Figures captions:

Fig. 1: (a) XRD patterns of undoped and Cu-TiO_2 powders annealed at 600°C. (b) Enlarged view of the XRD patterns around the anatase (101) reflection (c) same for the (200) reflection.

Fig. 2: Crystallite size (a) and full-width at half-maximum (FWHM) estimation of the anatase (101) and rutile (110) peaks (b) for pure TiO_2 and Cu-TiO_2 powders annealed at 400°C and 600°C versus Cu doping levels.

Fig. 3: Copper distribution characteristics in 3at.% Cu-TiO_2 samples annealed at 400°C. (a) TEM micrograph and corresponding fast Fourier transform (FFT) pattern from a typical area. (b) HAADF image showing a nanometer size copper particle (arrow). (c) Ti, (d) O and (e) Cu elemental maps from the area displayed in (b). (f) associated EELS Cu-$L_{2,3}$ to the areas labelled (1) and (2) in (e).

Fig. 4: Copper distribution characteristics in 6at.% Cu-TiO_2 samples annealed at 400°C. (a) TEM micrograph and the corresponding fast Fourier transform (FFT) pattern from a typical area. (b) HAADF image showing a large number of Cu particles decorating at grain boundaries or decorating the grain surface. (c) Ti and (d) Cu elemental maps from the area displayed in (b). (e) thresholding of the Cu map in order to separate the nanoparticles (visible in red) from the grain boundaries (in green). (f) the EELS Cu-$L_{2,3}$spectra summed over the corresponding nanoparticle pixels (1) and that at grain boundaries (2).

Fig. 5: Copper distribution characteristics in 3at.% Cu-TiO_2 samples annealed at 600°C. (a) HAADF image and (b) Cu-$L_{2,3}$ intensity map with thresholding from a protruding grain to isolate the spectroscopic contribution from the nanoparticles (in red) to that from the grain surface and boundaries (in green). (c) associated Cu-$L_{2,3}$spectra. (d) HAADF image of several adjacent grains. (e) Composite image after VCA processing of a spectrum image acquired from a reduced area and in the energy range of Ti-$L_{2,3}$ and OK edges. The blue, red and green pixels correspond to different TiO_2 phases. (f) VCA component EELS spectra associated to (e). (g) VCA component map associated to Cu, extracted from a spectrum image from the same reduced spatial area but encompassing the whole energy range of Ti-$L_{2,3}$, OK and Cu-$L_{2,3}$ edges. (h) Cu-$L_{2,3}$ edge associated to the VCA map displayed in (g).

Fig. 6: EELS for Cu-TiO_2 powders annealed at 400 (Cu 3 at.%, Cu 6 at.%) and 600°C (Anatase: Cu 3 at.% (A), Rutile: Cu 3 at.% (R), grain boundaries Cu 3 at.% (GB) and Cu 6 at.%). (a) Ti-$L_{2,3}$ ELNES. (b) OK ELNES.

Fig. 7: EPR spectroscopy of Cu-TiO_2 catalysts annealed at 400°C. EPR signal for (a) divalent copper ions (Cu^{2+}) and (b) oxygen vacancies (Vo). (c) Evolution of the peak-to-peak height of both signatures as a function of Cu doping levels.

Fig. 8: Plots of $(F(R).h\gamma)^{1/2}$ versus $h\gamma$ for estimating the band gap energies for sol gel undoped and Cu-TiO_2 powders annealed at 400°C (a) and 600°C (b), insets display the absorption spectra. (c) Evolution of the direct and indirect band gap energy estimation versus Cu incorporated levels.

Fig. 9: MB degradation by radiocatalysis using pure and Cu-TiO_2 catalyst annealed at 400° C (a) and 600°C (b).

Fig.1

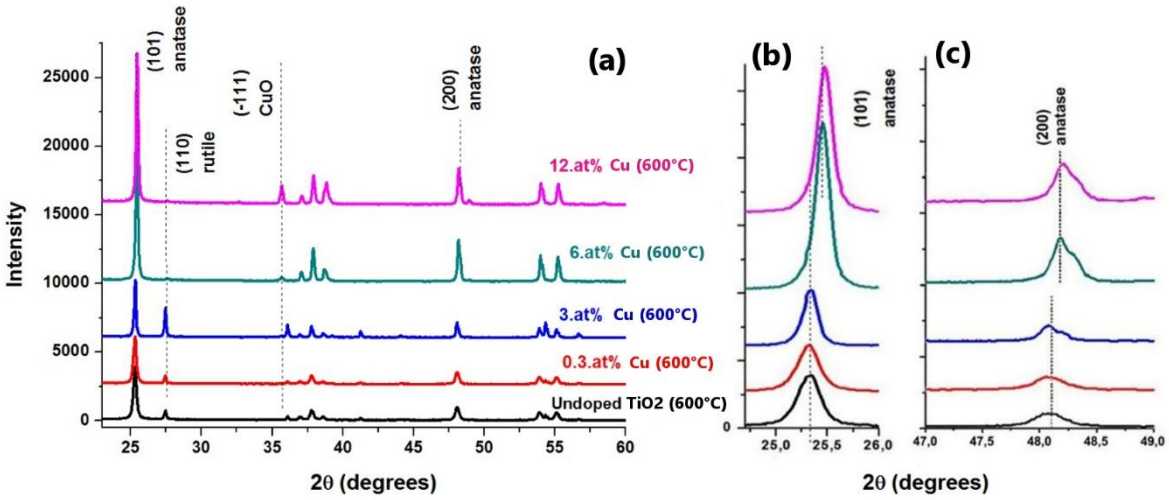
(a)
(b)
(c)
(101) anatase
(110) rutile
(-111) CuO
(200) anatase
12.at% Cu (600°C)
6.at% Cu (600°C)
3.at% Cu (600°C)
0.3.at% Cu (600°C)
Undoped TiO2 (600°C)
Intensity
2θ (degrees)
2θ (degrees)

Fig.2

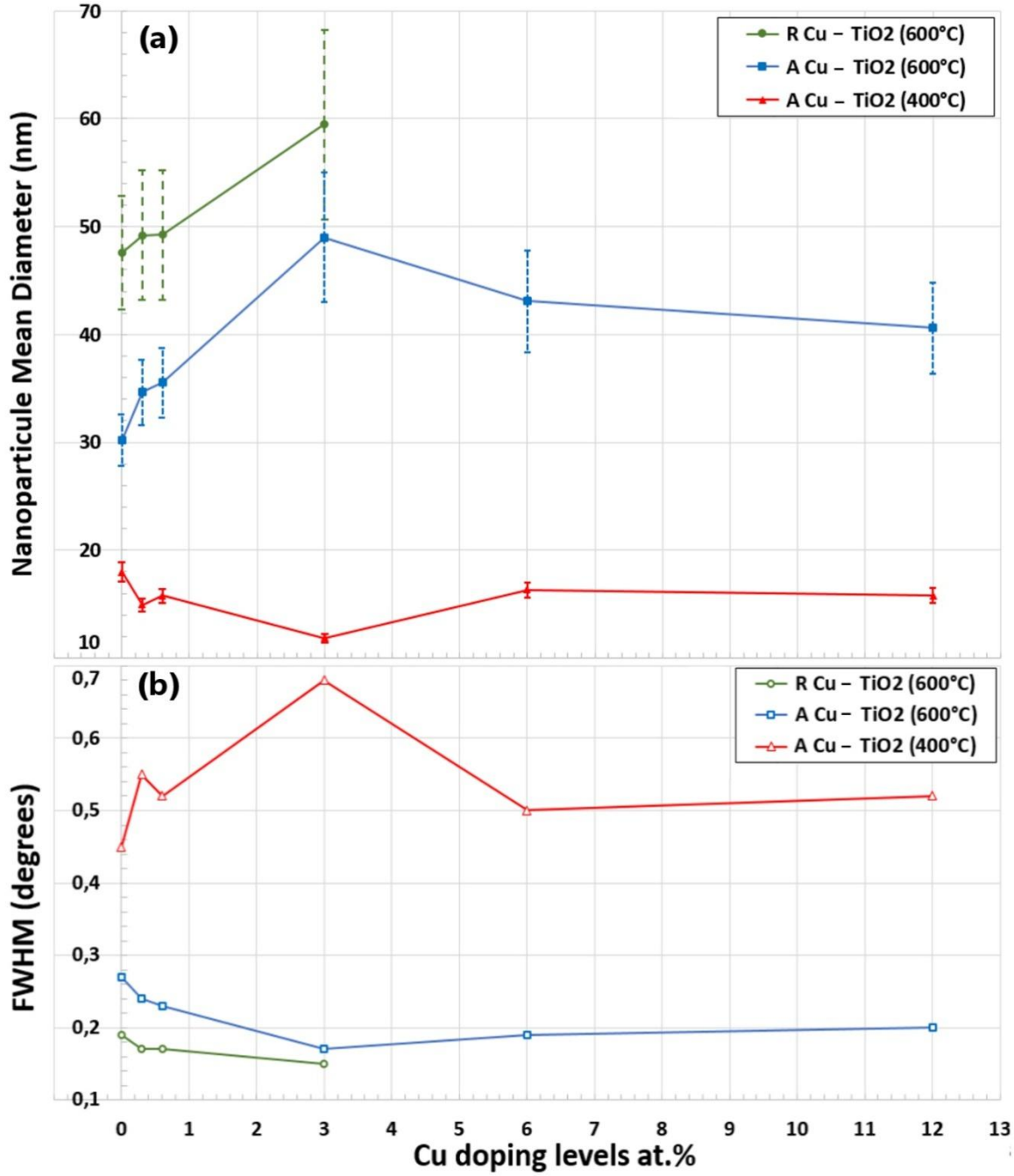
(a)
R Cu – TiO2 (600°C)
A Cu – TiO2 (600°C)
A Cu – TiO2 (400°C)
Nanoparticule Mean Diameter (nm)
70
60
50
40
30
20
10
(b)
R Cu – TiO2 (600°C)
A Cu – TiO2 (600°C)
A Cu – TiO2 (400°C)
FWHM (degrees)
0,7
0,6
0,5
0,4
0,3
0,2
0,1
0 1 2 3 4 5 6 7 8 9 10 11 12 13
Cu doping levels at.%

Fig.3

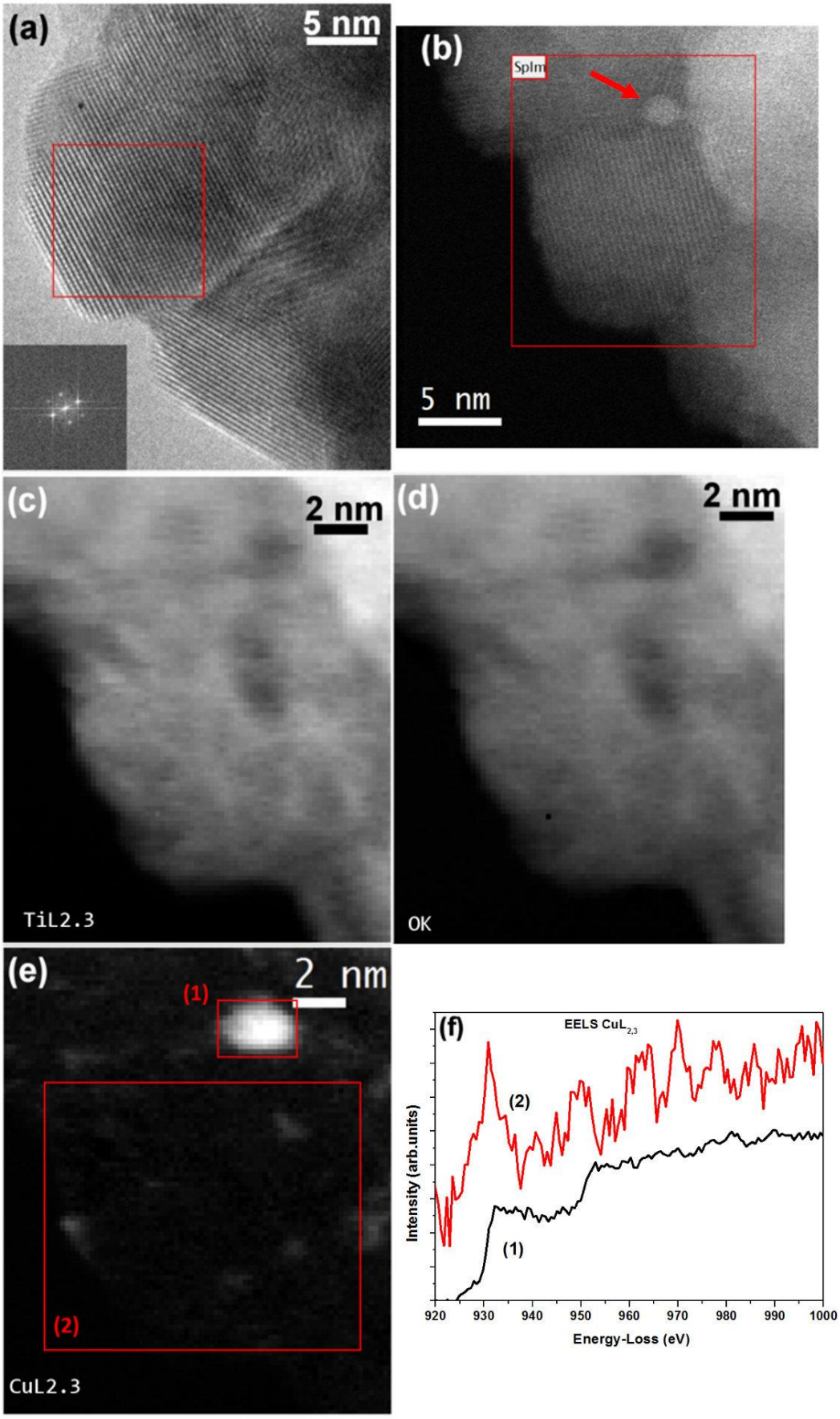
(a)
5 nm
(b)
SpIm
5 nm
(c)
2 nm
TiL2.3
(d)
2 nm
OK
(e)
2 nm
(1)
(2)
CuL2.3
(f)
EELS CuL2,3
(2)
(1)
Intensity (arb.units)
920
930
940
950
960
970
980
990
1000
Energy-Loss (eV)

Fig.4

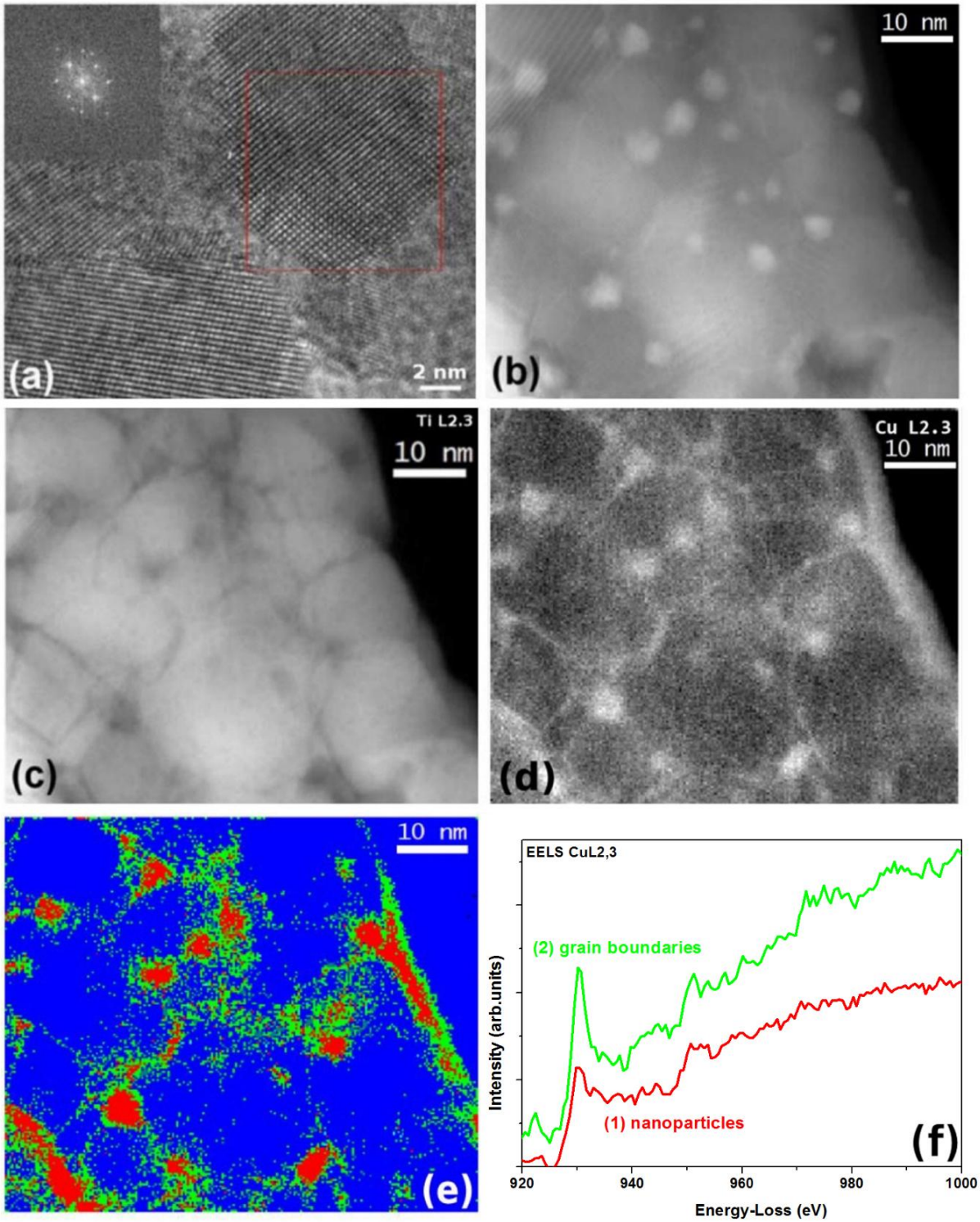
(a)
2 nm
(b)
10 nm
(c)
Ti L2.3
10 nm
(d)
Cu L2.3
10 nm
(e)
10 nm
EELS CuL2,3
(2) grain boundaries
(1) nanoparticles
(f)
Intensity (arb.units)
920
940
960
980
1000
Energy-Loss (eV)

Fig.5

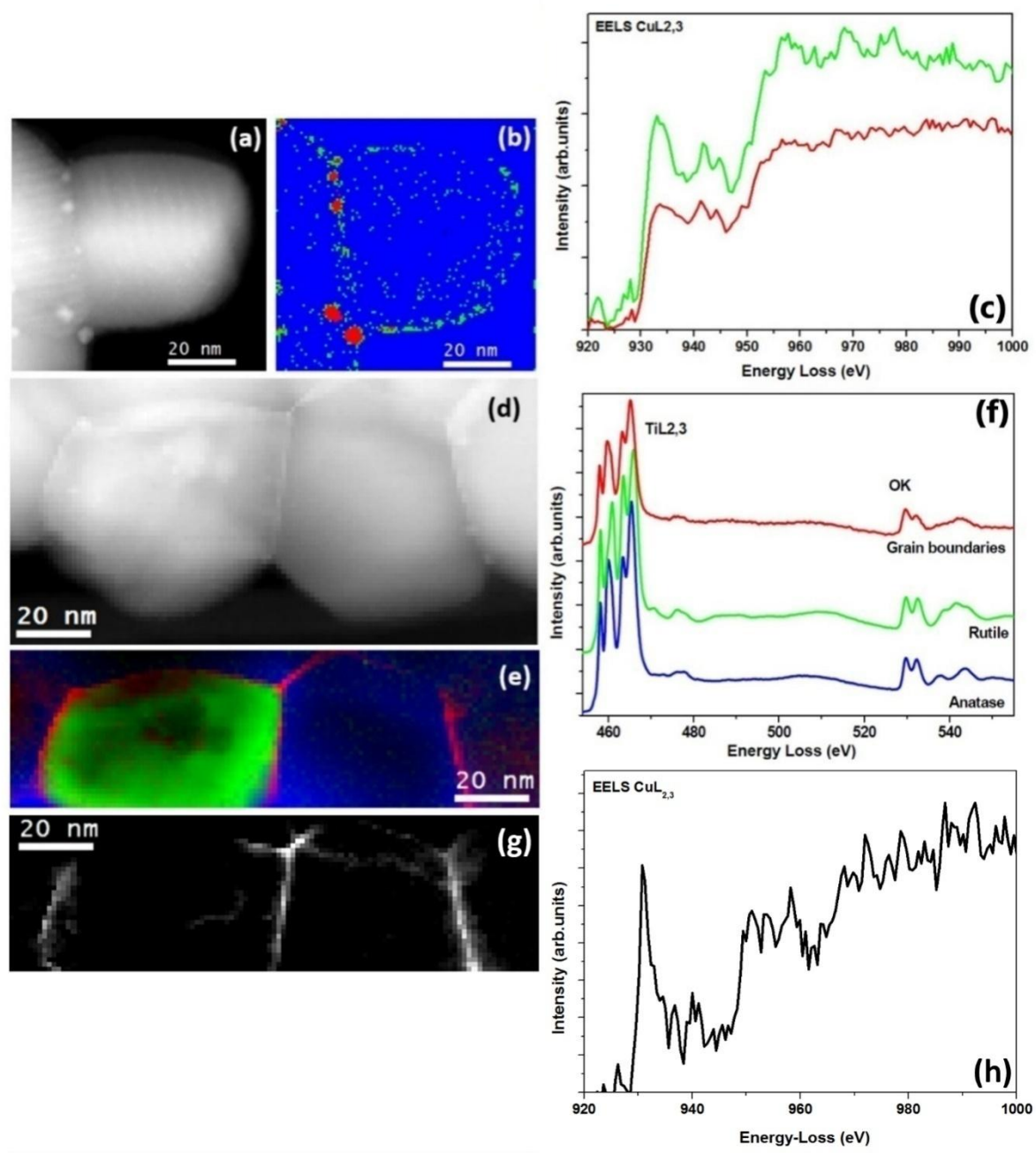
(a)
20 nm
(b)
20 nm
(c)
EELS CuL2,3
Intensity (arb.units)
920 930 940 950 960 970 980 990 1000
Energy Loss (eV)
(d)
20 nm
(e)
20 nm
(f)
TiL2,3
OK
Grain boundaries
Rutile
Anatase
Intensity (arb.units)
460 480 500 520 540
Energy Loss (eV)
20 nm
(g)
EELS CuL2,3
Intensity (arb.units)
(h)
920 940 960 980 1000
Energy-Loss (eV)

Fig.6

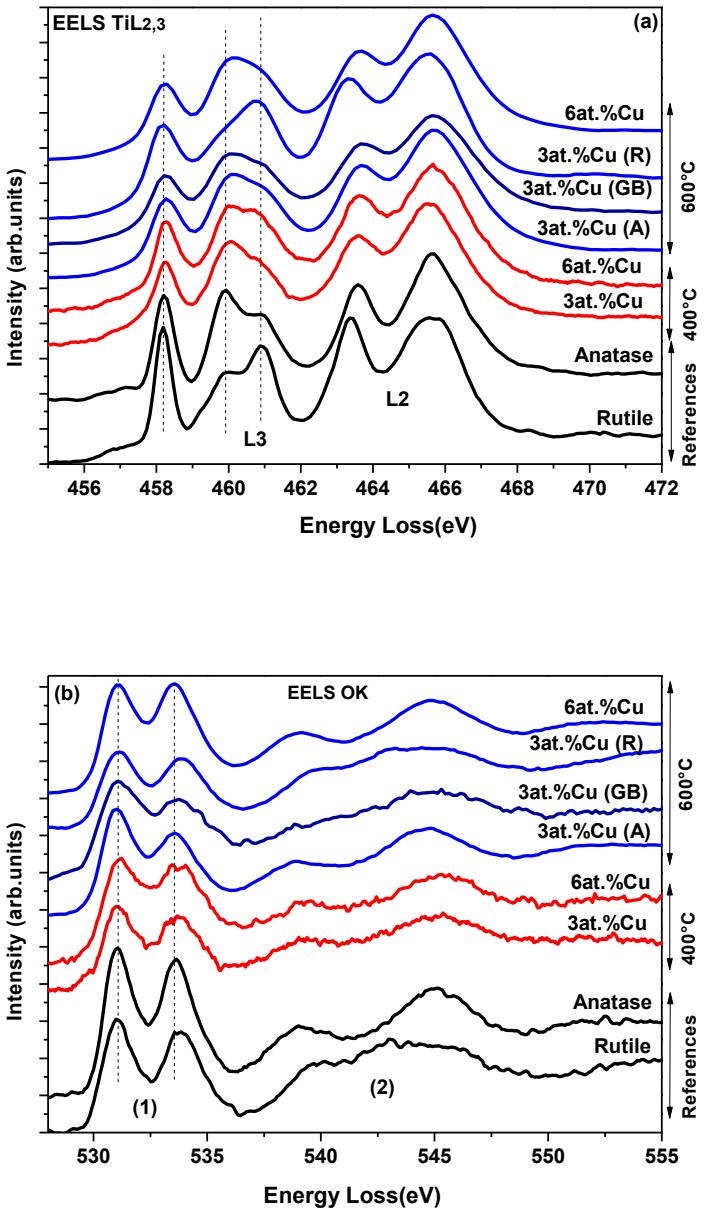
EELS TiL2,3
(a)
6at.%Cu
3at.%Cu (R)
3at.%Cu (GB)
3at.%Cu (A)
6at.%Cu
3at.%Cu
Anatase
Rutile
L3
L2
600°C
400°C
References
Intensity (arb.units)
456
458
460
462
464
466
468
470
472
Energy Loss(eV)
(b)
EELS OK
6at.%Cu
3at.%Cu (R)
3at.%Cu (GB)
3at.%Cu (A)
6at.%Cu
3at.%Cu
Anatase
Rutile
(1)
(2)
600°C
400°C
References
Intensity (arb.units)
530
535
540
545
550
555
Energy Loss(eV)

Fig.7

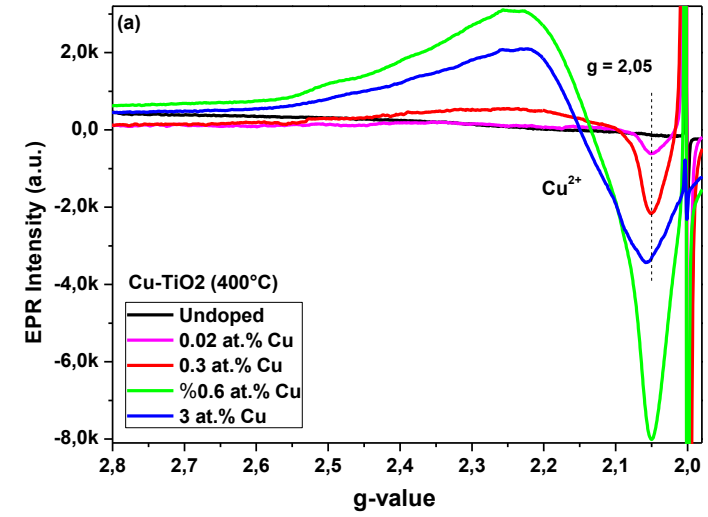
(a)
g = 2,05
Cu2+
Cu-TiO2 (400°C)
Undoped
0.02 at.% Cu
0.3 at.% Cu
%0.6 at.% Cu
3 at.% Cu
EPR Intensity (a.u.)
g-value

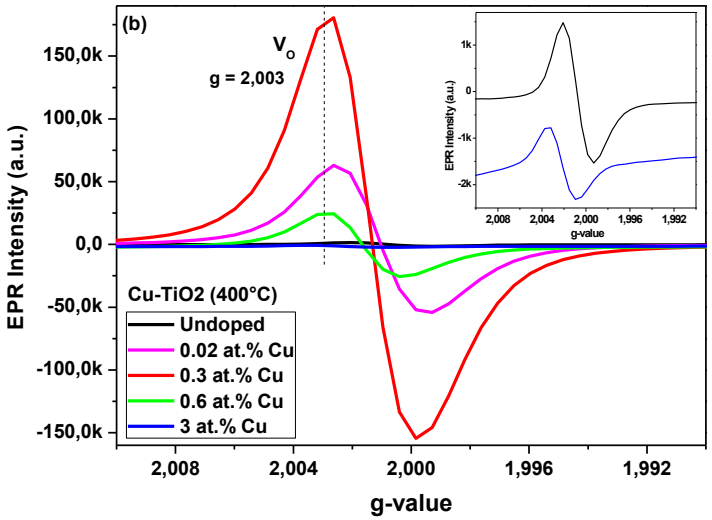
(b)
Vo
g = 2,003
Cu-TiO2 (400°C)
Undoped
0.02 at.% Cu
0.3 at.% Cu
0.6 at.% Cu
3 at.% Cu
EPR Intensity (a.u.)
g-value

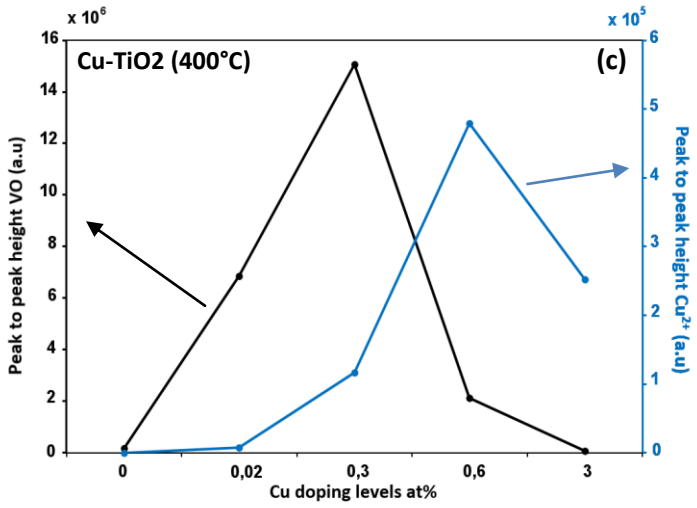
Cu-TiO2 (400°C)
(c)
Peak to peak height VO (a.u)
Peak to peak height Cu2+ (a.u)
Cu doping levels at%

Fig.8

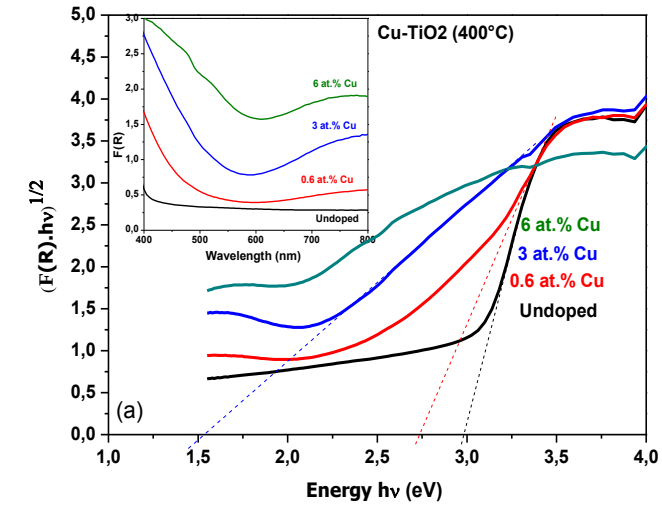
Cu-TiO2 (400°C)
6 at.% Cu
3 at.% Cu
0.6 at.% Cu
Undoped
(a)
(F(R).hν)^1/2
Energy hν (eV)
F(R)
Wavelength (nm)

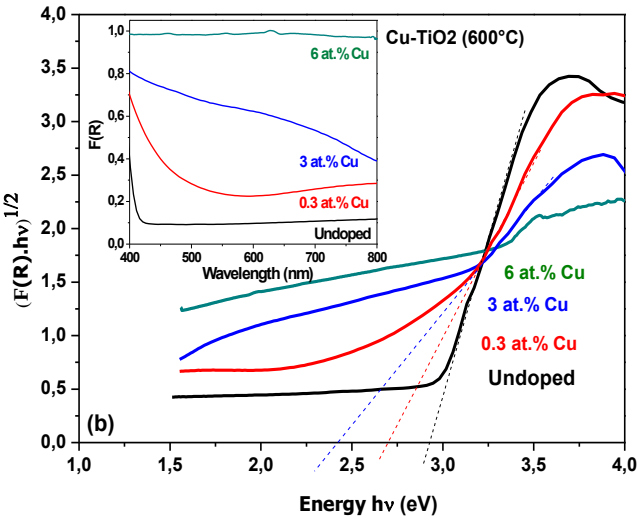
Cu-TiO2 (600°C)
6 at.% Cu
3 at.% Cu
0.3 at.% Cu
Undoped
(b)
(F(R).hν)^1/2
Energy hν (eV)
F(R)
Wavelength (nm)

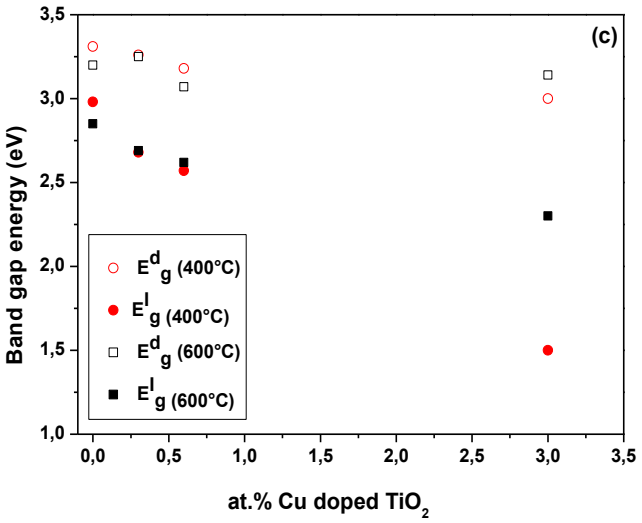
(c)
Band gap energy (eV)
at.% Cu doped TiO2
E^d_g (400°C)
E^I_g (400°C)
E^d_g (600°C)
E^I_g (600°C)

Fig.9

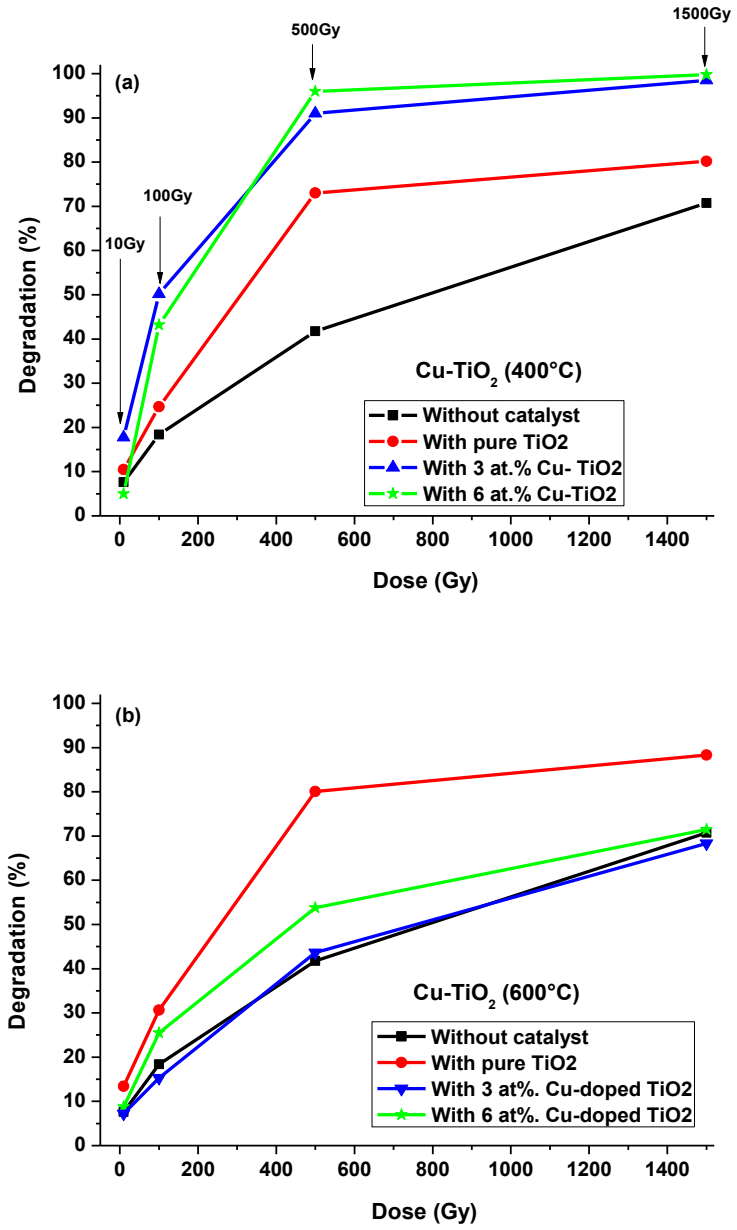
(a)
500Gy
1500Gy
100Gy
10Gy
Degradation (%)
Dose (Gy)
Cu-TiO2 (400°C)
Without catalyst
With pure TiO2
With 3 at.% Cu- TiO2
With 6 at.% Cu-TiO2
(b)
Degradation (%)
Dose (Gy)
Cu-TiO2 (600°C)
Without catalyst
With pure TiO2
With 3 at%. Cu-doped TiO2
With 6 at%. Cu-doped TiO2